Available online at www.sciencedirect.com
ScienceDirect
International Journal of Heat and Mass Transfer 50 (2007) 4948–4966
International Journal of HEAT and MASS TRANSFER
www.elsevier.com/locate/ijhmt

The Nukiyama curve in water spray cooling: Its derivation from temperature–time histories and its dependence on the quantities that characterize drop impact

Michele Ciofalo *, Antonino Caronia, Massimiliano Di Liberto, Salvo Puleo

Dipartimento di Ingegneria Nucleare, Università degli Studi di Palermo, Viale delle Scienze, I-90128 Palermo, Italy

Received 29 January 2007; received in revised form 17 September 2007
Available online 5 November 2007

Abstract

Heat transfer from hot aluminium walls to cold water sprays was investigated. The method used was the transient two-side symmetric cooling of a planar aluminium target, previously heated to temperatures of up to 750 K, by twin sprays issuing from full-cone swirl spray nozzles of various gauge. The target's mid-plane temperature was recorded during the cooling transient by thin-foil K thermocouples and a high-frequency data acquisition system. In order to determine the wall temperature T_w, the wall heat flux q''_w and the $q''_w - T_w$ heat transfer (Nukiyama) curve, two different approaches were used: the first was based on the solution of an inverse heat conduction problem, the second on a suitable parameterization of the Nukiyama curve and on the solution of a minimum problem. Relevant heat transfer quantities, such as the critical heat flux and the single-phase heat transfer coefficient, were obtained from each heat transfer curve. Their dependence on the main parameters characterizing the spray impact phenomenon (mass flow rate, drop velocity and drop diameter) was investigated on the basis of a preliminary hydrodynamic characterization study, and suitable correlations were proposed.

Keywords: Spray cooling; Induction heating; Inverse problem; Optimization algorithm

1. Introduction

1.1. Main characteristics of drops and sprays

Spray cooling is an effective method of heat removal and is used in a broad variety of engineering applications [1–5]. A large amount of experimental data and interpretative models have been gathered or developed through the years on all the stages of the phenomenon: drop generation and diameter/velocity distribution, drop–air interaction, impact and spreading mechanisms, drop-surface heat transfer.

Sprays can be produced by different devices (nozzles), corresponding to different types of energy responsible for the fragmentation of the liquid against its surface tension σ and for the ejection of the liquid drops with an exit velocity u_0. In particular, in *pressure* nozzles energy is provided by the pressure drop across narrow passages, often twisted so as to impart the liquid a swirling motion which promotes fragmentation and spatial uniformity (*swirl-jet* nozzles). Pressure nozzles can be classified according to the spatial distribution of the drops into *fan*, *hollow-cone* and *full-cone* nozzles [6]. These last are the most relevant for heat transfer purposes and have been the subject of the present investigation.

The drops in a spray are characterized by a size distribution, a velocity distribution, and a spatial distribution. Cross-correlations between size, velocity, and direction (i.e., angle formed with the spray axis) may also be of some relevance.

The size (diameter) distribution is often assumed to follow a *log-normal* law [7]:

* Corresponding author. Tel.: +39 91 232 225; fax: +39 91 232 215.
E-mail address: ciofalo@din.din.unipa.it (M. Ciofalo).

0017-9310/$ - see front matter © 2007 Elsevier Ltd. All rights reserved.
doi:10.1016/j.ijheatmasstransfer.2007.09.022

Nomenclature

a	dispersion parameter
A	area of an impact spot [m^2]
b	target side length [m]
b_i	coefficients of fifth-order polynomial
Bi	Biot number, $h\delta/k$
c_i	shape parameters of boiling curve
c_p	specific heat [$J\,kg^{-1}\,K^{-1}$]
C	heat capacity, Mc_p [$J\,K^{-1}$]
C_D	drag coefficient [–]
C_q	discharge coefficient [–]
d	generic diameter of a drop [m]
d_{32}	Sauter diameter of drops [m]
D	diameter of an impact spot [m]
E	root mean square error on $T_{mp}(t)$ [K]
F_D	drag force on a drop [N]
G	specific mass flow rate [$kg\,m^{-2}\,s^{-1}$]
h	generic heat transfer coefficient [$W\,m^{-2}\,K^{-1}$]
h_1	single-phase heat transfer coefficient [$W\,m^{-2}\,K^{-1}$]
J_{fg}	latent heat of vaporization [$J\,kg^{-1}$]
k	thermal conductivity [$W\,m^{-1}\,K^{-1}$]
L	distance from nozzle [m]
L_T	lightness threshold in digital image processing [–]
m	number of shape parameters
M	mass [kg]
MVD	median volume diameter of drops [m]
n	number of experimental points
p	pressure [$N\,m^{-2}$]
$p(\cdot)$	probability density function
q''	heat flux [$W\,m^{-2}$]
Q	total volume flow rate [$m^3\,s^{-1}$]
r_i	random numbers uniformly distributed in $[0,1]$
Re_a	Reynolds number of drop in air, ud/ν_a [–]
S	area for counting impact spots [m^2]
SS	nozzle type
t	time [s]
T	temperature [K]
u	generic velocity of a drop [ms^{-1}]
U	modal (and mean) velocity of drops [ms^{-1}]
V	volume [m^3]
We	Weber number, $\rho\,du^2/\sigma$ [–]

Greek symbols

α	thermal diffusivity [$m^2\,s^{-1}$]
δ	target half-thickness [m]
Δc_i	step amplitudes in parameter space
Δp	pressure head [$N\,m^{-2}$]
Δt	time step [s]
ΔT	temperature difference [K]
Δx	grid size along x [m]
ϑ	exposure time for drop impact method [s]
ϕ	spray cone semi-aperture angle [radians]
ρ	density [$kg\,m^{-3}$]
ρ_{el}	electrical resistivity [$\Omega\,m$]
σ	surface tension [$N\,m^{-1}$]
τ	conductive time constant, δ^2/α [s]
∇E	gradient of error E in parameter space

Subscripts

a	air
Al	aluminium
c	critical, or DNB (maximum heat flux)
f	fluid (water)
id	ideal
k	generic drop; generic experimental point
L	Leidenfrost (relative minimum of heat flux)
m	mean (average)
max	maximum
min	minimum
mp	mid-plane
M	modal
sat	saturation
w	wall
0	initial
1, 2	different points or regions in parameterized Nukiyama curve

$$p(\xi) = C\exp[-(\xi-\xi_M)^2/(2a^2)] \tag{1}$$

in which $\xi = \ln(d)$, C is a normalizing factor, a is a dispersion parameter, and $\xi_M = \ln(d_M) + a^2$ if d_M is the *modal* value of d, i.e., the value for which $p(d) = p(\xi)/d$ attains its maximum.

Different averages can be used to characterize drop diameters. A general definition [8] is

$$d_{NM} = \left[\frac{\int_0^\infty d^N p(d)\,\mathrm{d}d}{\int_0^\infty d^M p(d)\,\mathrm{d}d}\right]^{1/(N-M)} \tag{2}$$

with N and M positive integers in the range 0–3. The one most commonly used is d_{32}, or Sauter diameter, which preserves the surface to volume ratio of the actual distribution. Another commonly used parameter is the *median volume diameter MVD*, such that half the spray volume is contained in drops having $d \geqslant$ MVD and half in smaller drops. For drop populations following the log-normal distribution in Eq. (1) and having typical values of the a/ξ_M ratio, the Sauter diameter is slightly smaller than the median volume diameter (e.g., $d_{32} \approx 0.8$MVD) while the modal diameter d_M may be even several times smaller. Typically, 95% of the spray volume (hence, of its cooling capacity) is associated to drops ranging in diameter about nine fold between MVD/3 and 3MVD; these will be regarded in the following as the practical limits of the diameter spread. Techniques have been proposed to generate monodispersed sprays in

which all drops have roughly the same diameter and which may be more effective for specific cooling applications [9].

As regards the velocity dispersion, the speed of the liquid jet issuing from a pressure spray nozzle *before* its fragmentation into drops can be expressed as

$$u_0 = C_q(2\Delta p/\rho)^{1/2} \tag{3}$$

in which Δp is the pressure head and C_q is a discharge coefficient <1 which depends on the nozzle structure. For high Weber numbers (see below) the fraction of kinetic energy converted into surface energy is negligible, so that drops of all diameters can be assumed to leave the nozzle with the same velocity u_0. Further drop–air and drop–drop interactions may cause some velocity scatter; at some distance from the nozzle, u follows a normal distribution around a modal value U for any drop diameter, and is positively correlated with d [5].

As regards the spatial distribution of the spray, for a uniformly distributed, conical jet of total volume flow rate Q and semi-aperture angle ϕ the specific mass flow rate impacting normally on a small target located on the spray axis and at a distance L from the nozzle is:

$$G = \frac{\rho Q}{2\pi L^2(1-\cos\varphi)} \tag{4}$$

However, even full-cone sprays are *not* uniformly distributed, but exhibit some peaking of the angular mass flow distribution near the spray axis with a more or less steep fall at the edges. Therefore, G does *not* exactly follow a $1/L^2$ law, especially at small distances. This justifies the careful measurement of the specific flow rate at various distances which was conducted in the present study as will be discussed in Section 3.

An *individual* spherical drop is fully characterized by its physical properties, its diameter d, and its velocity u. These quantities are often grouped into different dimensionless numbers, among which a particular relevance has the *Weber number*:

$$We = \frac{\rho \cdot d \cdot u^2}{\sigma} \tag{5}$$

The Weber number is 12 times the ratio of the kinetic energy of the drop $Mu^2/2$ to the surface energy σS (energy required to create the drop surface by bulk liquid fragmentation). Drop impact against a solid surface is dominated by inertial forces for $We \gg 1$, by surface forces for $We \ll 1$. As will be discussed later, the water drops in the present study presented a practical diameter spread between $\sim 0.12\times10^{-3}$ and $\sim 6\times10^{-3}$ m and velocities between $\sim$15 and $\sim$50 m/s, smaller diameters being obtained for larger pressure heads and thus for higher velocities. As a consequence, We ranged between $\sim$1200 and $\sim$ 70,000 and drop impact phenomena were inertia-dominated in all cases. For the same reason, the fraction of pressure energy converted into surface energy was negligible as compared with that converted into kinetic energy or dissipated by frictional losses.

1.2. Drop–air interaction

Drop–air interactions determine the extent to which the drop velocity, mass and temperature vary along the drop path and thus depend on the nozzle-target distance.

The drag force on a spherical drop of diameter d can be expressed as:

$$F_D = C_D\frac{\pi d^2}{4}\rho_a\frac{u^2}{2} \tag{6}$$

in which ρ_a is the density *of air* and the drag coefficient C_D depends on the Reynolds number $Re_a = ud/\nu_a$. Piecewise correlations for C_D are not appropriate here since Re_a may be as high as 2500 at the nozzle exit, but decreases to the small value associated with the terminal free fall velocity as the drop is slowed down by friction with air. A simple correlation which fits fairly well most classic experimental results in a wide range of Re_a values is [10]:

$$C_D = \frac{24}{Re_a}(1+0.02Re_a) \tag{7}$$

By substituting Eq. (7) for C_D into Eq. (6) and taking account of the gravity acceleration, the drop velocity and trajectory are easily obtained by numerical integration. Results are shown in Fig. 1 for two values of the initial velocity u_0, 20 and 50 m/s, roughly covering the range of conditions of the present tests.

Fig. 1a shows the drop trajectory for different values of d (from 10^{-4} to 10^{-3} m) and $u_0 = 20$ m/s or 50 m/s. Drops with $d \geqslant 10^{-3}$ m practically follow the parabolic path that would characterize a massive body with initial horizontal velocity u_0. For such drops, at the largest nozzle-target distance considered in the present study (0.4 m) the vertical deflection is negligible. Smaller drops, however, deviate significantly from this behaviour; at $x = 0.4$ m, drops with $d = 2\times10^{-4}$ m are deflected by gravity almost 2×10^{-2} m for $u_0 = 20$ m/s, and drops with $d = 10^{-4}$ m or less are likely never to reach the target for both values of the initial velocity.

Fig. 1b reports the drop speed (including the vertical component due to gravity) as a function of the distance x from the nozzle for the same diameters and the same values of the initial velocity. For each diameter, there is a limit speed which coincides with the terminal free fall velocity in air and, of course, does not depend on u_0. However, the maximum horizontal displacement *does* depend, albeit weakly, on the initial velocity; for example, for drops 5×10^{-4} m in diameter, this is about 3.2 m for $u_0 =$ 20 m/s and 4.5 m for $u_0 = 50$ m/s. At $x = 0.4$ m, even large drops ($d = 10^{-3}$ m) are slowed down by more than 15% for $u_0 = 20$ m/s and about 8% for $u_0 = 50$ m/s. For smaller drops, e.g., $d = 2\times10^{-4}$ m, at a distance of 0.4 m the velocity is reduced by a factor of $\sim$7 for $u_0 = 20$ m/s and of $\sim$3 for $u_0 = 50$ m/s. The smallest drops ($d = 10^{-4}$ m or less) are stopped by drag within 0.2–0.3 m and at this distance possess just their terminal (purely vertical) velocity in air.

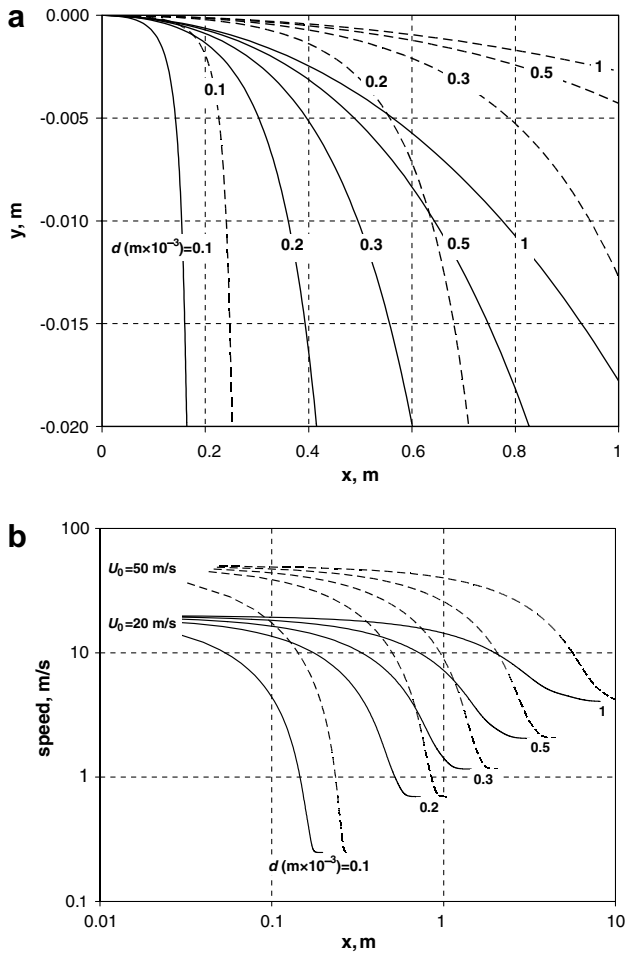

Fig. 1. Trajectory (a) and speed (b) for drops of different diameters. Solid lines: $u_0 = 20$ m/s; broken lines: $u_0 = 50$ m/s. Based on the drag correlation in Eq. (7).

As mentioned above, the drop diameter and (initial) velocity range of interest in the present study corresponds to $d = (1/3–3)\mathrm{MVD} = 1.2 \times 10^{-4}$ to 6×10^{-3} m and $u =$ 15–50 m/s, with d and u negatively correlated *via* the dependence of both MVD and U upon the pressure head Δp. On the basis of the results in Fig. 1, it can be observed that, especially for the larger nozzle-target distances considered in the present study (0.3–0.4 m), the braking effect of air will practically filter out the smallest drops. The *direct* influence of this selective filtering on the specific mass flow rate G hitting the target at various distances, which is the main parameter affecting heat transfer, is small because the smallest drops carry a negligible fraction of the spray's mass; in any case, it was implicitly taken into account by the *in situ* characterization procedure described in Section 3, i.e., by explicitly measuring the values of G for each operating condition. However, more subtle, *indirect* effects can not be ruled out, such as the influence of drop filtering on the correlation between heat transfer quantities and drop velocity and diameter. Also coalescence and scattering between faster, larger drops and slower, small ones may play a role. Another consequence of the velocity-diameter correlation is that the flow rate hitting the target will increase gradually, rather than stepwise, during the first instants of cooling, as drops with different velocities reach the target with variable delays after the valves on the nozzles are open.

A thorough analysis of these effects is beyond the scope of the present work. Suffice it to say that results obtained for the larger nozzle-target distances and the more finely dispersed sprays (i.e., larger pressure heads and/or small gauge nozzles) should be taken with some caution, especially concerning the initial stage of the cooling transients up to 0.02–0.03 s, which corresponds to the difference in flight time between small and large drops at the lowest outlet velocities and largest nozzle-target distances investigated.

As regards evaporative cooling, which may alter the mass and temperature of the drops during their flight from nozzle to target, it depends on the temperature and relative humidity of the surrounding air. In the present tests, it was kept to a minimum by limiting the nozzle-target distance to 0.4 m at most (flight time < 0.03 s), using water at ambient temperature ($\sim$296 K), and encasing the whole nozzle-spray-target system in a Perspex© enclosure that was practically saturated in humidity at all times.

1.3. Heat transfer

Heat transfer in spray cooling has been investigated by either steady state or transient methods. The former rely on a thermal balance between the power input into an appropriate sample and the heat transferred to the spray; their application is limited by the maximum attainable power densities. For example, in the present tests the target was a slab $75 \times 75 \times 4 \times 10^{-3}$ m in size, cooled from both sides with heat fluxes up to $\sim 10^7$ W/m^2. Therefore, a power input of $\sim 10^5$ W would have been required to keep it at a constant temperature, which was clearly unfeasible. Moreover, in power controlled systems steady state conditions cannot be maintained in the unstable region of the heat transfer curve (transitional boiling). Because of these limitations, steady state methods have usually been confined to investigations involving low mass flow and heat transfer rates (e.g., single streams of drops).

In transient tests, a target is typically heated to a uniform high temperature and then rapidly cooled by the spray while the temperatures at one or more inner locations are recorded. Surface heat flux and temperature can then be derived from the raw experimental data by various techniques [11,12]. The method is the only viable if large heat transfer rates are involved, and has been most commonly adopted in full-scale spray cooling research.

A review of the literature *ante* 1980 is given by Bolle and Moureau [5]. Data are reported for different nozzle types (fan *vs.* full cone) and pressure heads (from 0.1 to 15×10^6 N/m^2), yielding mass flow rates from 0.5 to 50 kg/(m^2 s), drop velocities from 10 to 100 m/s and drop Sauter diameters from $\sim 10^{-4}$ to 10^{-3} m. The studies

reported used either steady state or transient methods, and differed also in the geometry of the spray-surface arrangement.

Most of the above studies regard vertical sprays impacting (usually from above) on horizontal surfaces, which, of course, exhibit a different behaviour with respect to the vertical surface case considered in the present paper. Horizontal surfaces generally exhibit very high temperatures T_c of DNB (departure from nucleate boiling, corresponding to the maximum, or critical, heat flux q''_c) and high Leidenfrost temperatures T_L. For example, Hoogendoorn and den Hond [13] reported this latter quantity as a function of the specific mass flow rate G and of the mean drop velocity U for the spray cooling of horizontal stainless steel surfaces. For $U = 15$ m/s, T_L was found to increase from ~ 600 to ~ 1000 K as G increased from 0.6 to 30 kg/(m^2 s), while values ~ 100 K higher were obtained for a drop velocity of 30 m/s. Therefore, U appeared to have a significant independent influence on T_L. The Sauter drop diameter in these tests ranged from $\sim 0.2 \times 10^{-3}$ to $\sim 1 \times 10^{-3}$ m but did not appear to play a major role. Both the DNB temperature T_c and the critical heat flux q''_c were found to be heavily affected by the mass flow rate, increasing from ~ 508 K and $\sim 0.84 \times 10^6$ W/m^2 at $G = 0.6$ kg/(m^2 s) to ~ 773 K and $\sim 2.8 \times 10^6$ W/m^2, respectively, at $G = 25$ kg/(m^2 s).

The only studies for vertical surfaces reviewed by Bolle and Moureau are those by Junk [14], who used fan-type nozzles to cool stainless steel tubes, and by Müller and Jeschar [15], who used full-cone nozzles to cool stainless steel plates. Both studies were based on a steady-state technique and thus could not obtain the whole heat transfer curve. The former paper reported DNB temperatures above 420 K, critical heat fluxes above 1–2 $\times 10^6$ W/m^2, and Leidenfrost temperatures below 900–1100 K. In the film boiling region, it was found that, despite the complexity of this heat transfer regime in which radiation plays a role, the q''_w-ΔT_w relationship was roughly linear, with heat transfer coefficients of the order of ~ 400 to ~ 800 W/(m^2 K) increasing about linearly with the mass flow rate. However, a more than linear behaviour was found in the latter paper, with heat transfer coefficients similar to the above figures at ~ 1100 K but increasing with the wall temperature.

More recently, Yao and co-workers [16,17] focused their attention on the Leidenfrost transition and on the film boiling regime in the cooling of hot walls by horizontal and vertical-downward water sprays. Typical values of the hydrodynamic parameters were $G \approx 0.3$–2 kg/(m^2 s), $U \approx 3$–4 m/s and $d_{32} \approx 0.5 \times 10^{-3}$ m. Maximum heat fluxes of up to 2×10^6 W/m^2 were measured for wall temperatures of 410–430 K, while the Leidenfrost point temperature was about 530 K. The influence of spray-wall orientation and the relative importance of conduction, convection and radiation were analyzed. The influence of air flow on heat transfer in pneumatic sprays was also discussed.

Ghodbane and Holman [18] conducted spray cooling tests using Freon-113 refrigerant instead of water. This allowed boiling at relatively low wall temperatures. Heat transfer correlations were derived in terms of the Weber number.

Hall and Mudawar [1] conducted measurements for specific mass flow rates G between 0.58 and 10 kg/(m^2 s), mean drop velocities U between 10 and 30 m/s, and drop diameters d_{32} between 0.137×10^{-3} and 1.35×10^{-3} m, conditions which are close to those of the present study. They proposed correlations for the temperature and heat flux at onset of nucleate boiling, departure from nucleate boiling and point of minimum heat flux (Leidenfrost), and correlations for the heat transfer coefficient h in all the regimes covered by the investigations, i.e., single-phase, nucleate boiling, transitional boiling and film boiling. In particular, they found that the DNB temperature varied little with the mass flow rate and the other spray parameters and ranged between 470 and 520 K, while the Leidenfrost temperature ranged between 590 and 730 K, was little sensitive to the specific mass flow rate and to the drop diameter, and increased weakly with the drop velocity.

With reference to the quantities that were explicitly determined in the present study, i.e., the single-phase heat transfer coefficient h_l and the maximum, or critical, heat flux q''_c, adopting the nomenclature of the present paper and using the physical properties of water at the temperature and pressure indicated by the authors, the correlations proposed by Hall and Mudawar can be expressed in SI units as:

$$h_l \approx 1029\, G^{0.76} d_{32}^{-0.24} \tag{8}$$

$$q''_c \approx 5.47 \times 10^5 G^{0.604} d_{32}^{-0.198} \tag{9}$$

Note that these do *not* explicitly contain the velocity of the drops. They indicate that both h_l and q''_c increase (at different rates) mainly with the specific flow rate G and decrease with the drop (Sauter) diameter d_{32}.

The study by Ciofalo et al. [19] focused on single-phase heat transfer and nucleate boiling at high specific mass flow rates. The experimental technique was similar to that described in the present paper (twin-spray transient cooling), but the target was made of a copper–beryllium alloy and the nozzle-target distance was fixed at 5×10^{-2} m. Only four nozzle types and three values of the pressure head were investigated. Values of G up to 80 kg/(m^2 s) were considered, giving wall heat fluxes in excess of 10^7 W/m^2 and cooling rates above 1000 K/s, while the wall temperature never exceeded 573 K (far below the Leidenfrost temperature expected at such high flow rates). Tentative correlations were proposed for the single-phase heat transfer coefficient and the critical heat flux.

2. Experimental method

2.1. Test rig and measurement technique

A complete description of the experimental rig and of the measurement technique has been given by Puleo [20].

The method involved the transient two-side symmetric cooling of a planar target, composed of two $75 \times 75 \times 10^{-3}$ m slabs of high-purity (99.999%) aluminium, each having a thickness δ of 2×10^{-3} m (see Table 1). The target was first heated to temperatures up to ~750 K and then cooled by twin sprays issuing from commercial nozzles of various gauges. In particular, four different types of full-cone, swirl-type spray nozzles were tested; they are manufactured by Spraying Systems Co. and will be indicated in the following as SS1, SS3, SS5, SS10. The nozzles, made of stainless steel, are identical in shape but differ in size, so that they are characterized by different values of the mass flow rate for a given pressure head; the number following "SS" expresses roughly the flow rate in litres per minute for a pressure head of 10^6 N/m^2. Distilled water at ambient temperature was used in all tests.

The test rig is schematically represented in Fig. 2. Besides target, data acquisition system and dedicated PC, its main components are: a pneumatic ejector, composed of an air-filled stainless steel cylinder and a water-filled rubber balloon, dimensioned for pressures up to 6.4×10^6 N/m^2; a nozzle traversing device allowing nozzle-target distances L up to 0.4 m; an induction heater; a target lifting device, allowing the target to be moved from the heating position between the polar expansions of the induction heater to the cooling position between the nozzles; and a Perspex© enclosure.

Table 1
Geometry and physical properties at 300 K of the Al target [23]

Side length	b	0.075	m
Half thickness	δ	2×10^{-3}	m
Density	ρ	2702	kg m^{-3}
Thermal conductivity	k	237	W m^{-1} K^{-1}
Specific heat	c_p	903	J kg^{-1} K^{-1}
Electrical resistivity	ρ_{el}	26.5×10^{-9}	Ω m
Derived quantities:			
Volume	$V = b^2 s$	22.5×10^{-6}	m^3
Mass	$M = \rho V$	60.7×10^{-3}	kg
Heat capacity	$C = Mc_p$	54.9	J K^{-1}

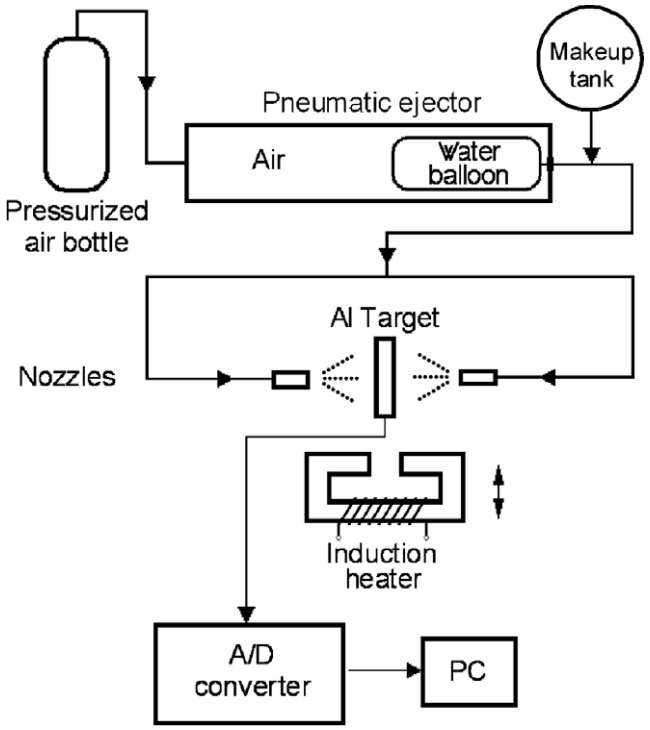

Fig. 2. Schematic representation of the test rig.

The mid-plane target temperature T_{mp} was measured during the cooling stage by three thin-foil K-type thermocouples having a thickness of 12.7×10^{-6} m and thus a negligible time constant. These were connected in series to increase the voltage output, thus reducing the relative importance of noise. The signal was recorded at a frequency of 5000 s^{-1} by a 16-bit A/D converter and pre-amplifier. In order to reduce random fluctuations, data were further averaged five by five before being permanently stored into data files, which thus contained 1000 measurements per second. A physical cold junction was adopted (melting ice in a Dewar jar) to reduce inaccuracies and NIST thermocouple data [21] were used to convert voltage output into temperatures.

The pneumatic ejector with separated fluids was preferred to simpler alternative methods (such as using a centrifugal pump) because it provides a more uniform flow rate during the discharge and allows the working fluid (water) to be kept gas-free. Hand operated spherical valves were simply used to supply water to the spray nozzles. Data acquisition started some time (~1 s) before the opening of these valves and the real initial instant of the cooling transient (as defined by the first drop impacts on the target's surface). A separate J-type thin-foil thermocouple, placed immediately below the target at the same distance from one of the nozzles and also connected to the data acquisition system, was used to signal this initial instant. When appropriate (i.e., in conjunction with the inverse conduction problem method, see below), previous data, recording only the slow cooling of the target in air, were retained in the time series until filtering so as to avoid edge problems, and were then discarded.

For each test, data acquisition was terminated after a cooling time typically varying between 5 and 25 s (according to the specific test conditions), when the mid-plane temperature was practically coincident with the fluid and ambient temperature T_f. In most cases, the significant phase of the transient, during which the wall-fluid temperature difference dropped from the initial value of 400–450 K to a few K, last only 1–5 s. The pneumatic ejector was dimensioned in such a way that the volume of water ejected during this time was a small fraction (<5%) of the total volume of the ejector. This ensured that the pressure head, and thus the mass flow rate, decreased by less than 5% and 2.5%, respectively, during the significant phase of the cooling transient. Some influence of the pressure fall on the "tail" of the temperature-time history, and thus on the values derived for the single-phase heat transfer coefficient, is

expected only in the test cases characterized by relatively low heat transfer rates (hence, long transients) combined with high *total* flow rates (high pressure heads – larger nozzles). These cases correspond to the larger nozzle-target distances, in particular $L = 0.4$ m.

Following each test, the volume of water in the rubber balloon was restored by a purpose built make-up apparatus including a high pressure hand pump and a calibrated cylinder. Tests were repeated several times for each experimental condition, defined by type of nozzles SS, pressure head Δp and nozzle-target distance L. Records were discarded when the quality of the data was obviously poor due to excessive electromagnetic noise or operational errors. A minimum of three valid tests were obtained for each experimental condition, and the heat transfer quantities derived from the corresponding temperature-time histories were then averaged to obtain the relevant values for each experimental condition.

2.2. Induction heating

In our previous investigation [19], the target was radiatively heated by quartz resistors. This method allowed only temperatures up to ~ 570 K to be attained, required long heating-up times ($\sim 10^3$ s), and caused also the surrounding structures and the nozzles themselves to be heated, thus making the temperature of the first impacting drops uncertain.

In order to overcome the above limitations, an induction heating technique was chosen here, which allows power to be released rapidly and uniformly in the target's volume without heating the surrounding structures [22]. The heater was built by winding 1.25×10^{-3} m diameter coated copper wire around a transformer core (relative permeability ~ 750), $40 \times 50 \times 10^{-3}$ m in cross section and ~ 0.55 m in developed length. A 0.01 m gap was cut to accommodate the aluminium target. Calculations taking into account the mutual inductance of the coils, supported by preliminary tests, led to the choice of 4 concentric coils electrically connected in parallel, each including 217 windings (~ 50 m wire length per coil).

The power supply was a Variac auto-transformer, providing a maximum current intensity of 20 A at 160 V for a maximum total (active + reactive) power of 3.2×10^3 VA. Thermal measurements provided an estimate of $\sim 10^3$ W for the thermal power which was actually dissipated at 300 K in the target volume of 22.5×10^{-6} m^3 (power density $\sim 44 \times 10^6$ W/m^3) when the total power provided by the source was 2×10^3 VA. Thus, the heating efficiency was $\sim 50\%$ at room temperature. As the temperature increased, the available heating power decreased rapidly due to the increase of the electrical resistivity of aluminium; an increasing fraction of it was released by radiation to the environment; and the temperature rate of rise was further reduced by the increase of the specific heat [23]. However, it was still possible to heat the target to ~ 720 K in ~ 60 s.

3. Hydrodynamic characterization of the sprays

The quantities which were independently made to vary in the cooling tests (control, or *external* parameters) are the nozzle type SS (range SS1...SS10), the nozzle–to-target distance L (from 0.1 to 0.4 m), and the pressure head Δp (from 0.2 to 2×10^6 N/m^2). On the other hand, on physical grounds one may assume that the heat transfer curve and its characteristic features (such as the critical heat flux q''_c and the single-phase heat transfer coefficient h_1) depend only on local, or *internal* quantities characterizing the impact of the drops upon the hot target surface, such as G (specific mass flow rate on the target), u (drop velocity or velocity distribution) and d (drop diameter or diameter distribution).

Therefore, a preliminary characterization study was conducted in order to clarify the dependence of the latter upon the former, i.e., to obtain the functional relations $G = G(\mathrm{SS}, \Delta p, L)$ and similar. Other variables which might potentially affect heat transfer, such as the water temperature and the surface finish of the target, were kept constant during the tests; their influence will be the subject of future studies.

3.1. Total and specific flow rate

Total and specific flow rates were easy to determine with a good accuracy by measuring volumes collected in a given time. Fig. 3 reports the total volumetric flow rate Q measured as a function of the pressure head for all four nozzle types investigated. Each experimental value is an average between the flow rates Q_A and Q_B issued from the two twin nozzles A and B when they operated simultaneously, as in the cooling tests. It was also checked that the difference between Q_A and Q_B in each run was never larger than 1–2%. As shown in the figure, experimental flow rates were well approximated by a $\Delta p^{1/2}$ power law (solid curves).

The variation of the *specific* mass flow rate G at the spray cone centreline (i.e., on the target) as a function of

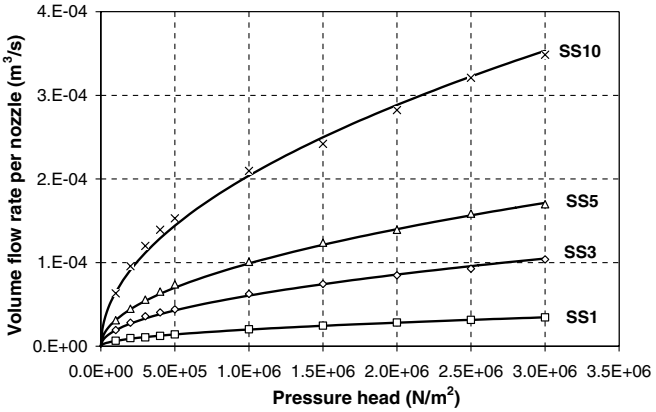

Fig. 3. Total volume flow rate as a function of the pressure head for all nozzles. Solid lines are best-fit curves following a 1/2 power law dependence on Δp.

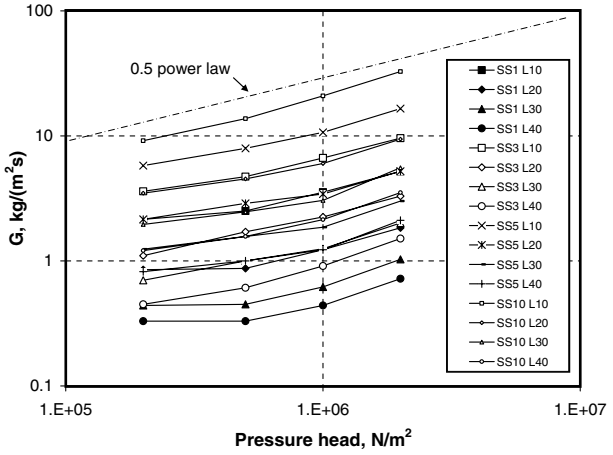

Fig. 4. Specific mass flow rate at spray centreline as a function of the pressure head for all nozzles.

the pressure head is more complex, due to the fact that a change in Δp affects not only the total flow rate (see above), but also the spray cone aperture and angular distribution. Results are summarized in Fig. 4 as measured by collecting the water through a circular aperture, 5×10^{-2} m in diameter, similar in area to the active region of the target. At low pressure heads G does not significantly change or even decreases slightly (nozzle SS1) with Δp, indicating that the increase in Q is accompanied by a considerable spreading of the spray cone, as confirmed by visual observations. On the other hand, at high pressure heads G increases more rapidly than $\Delta p^{1/2}$, indicating that higher values of Δp lead to a greater concentration near the spray centreline. This non-monotonic behaviour of the spray cone aperture with the pressure head is coherent with the manufacturer's data on the cone angle at different pressure heads.

3.2. Drop size

The experimental assessment of drop size and velocity distributions for different nozzles and pressure heads was more difficult. Only approximate results could be obtained, which, however, is acceptable because these quantities play only a secondary role in heat transfer as compared with that of the specific mass flow rate.

The numerical density of drops and their size distribution were estimated by an impact method [20]. Impact pits, or spots, were created by the drops in a thin (2–3×10^{-3} m) layer of foam deposited on a flat surface, which was exposed to the spray for a short time interval ϑ (typically, 1/160 s) in order to keep the number of impacts suitably low. A gravity-driven curtain shutter was used to this purpose.

Unfortunately, the drop size distribution at impact depends on L *via* the braking effects discussed in Section 1.2, which reduce the numerical flux of smaller drops on the target; therefore, a complete characterization should be repeated for each of the distances L used in the cooling tests. However, as Fig. 1 shows, these effects are significant only for drops of diameter less than 3×10^{-4} m, which are those that contribute less to mass flow rate and heat transfer. Therefore, the diameter characterization was performed only for an intermediate nozzle-target distance ($L = 0.2$ m) and the values thus determined for the median volume diameter were assumed to hold also at smaller or larger distances.

The resulting spot pattern was photographically recorded by a 6 Mpixel digital camera and then digitally processed by commercial image-processing software. The central portion of the image, corresponding to a rectangle having sides of 5×10^{-2} and 3×10^{-2} m, was selected for processing. It was converted into a binary (i.e., pure black and white) image by setting a lightness threshold L_T and was stored in pgm (*portable gray map*) numerical format. The pgm file was then processed by a purpose written Fortran© program which identified individual spots, evaluated their areas A_k and equivalent diameters $D_k = (4A_k/\pi)^{1/2}$, and built the corresponding size distribution. This was finally corrected in order to account for the difference between drop size and impact spot size by using the independently measured values of the mass flow rate G for the same combination $(SS, \Delta p, L)$. For this correction, proportionality was assumed (for a given drop speed) between the equivalent diameter D_k of an impact spot and the diameter d_k of the drop causing it. The proportionality factor was thus determined from:

$$\frac{D_k}{d_k} = \left[\frac{\rho \sum_k \pi D_k^3/6}{GS\vartheta}\right]^{\frac{1}{3}} \tag{10}$$

in which S is the surface area where impacts spots were counted (15×10^{-4} m^2), ϑ is the time during which this surface was exposed to the spray (1/160 s), and the summation is extended to all the impact spots identified by the above described digital image processing procedure. Values of ~2–3 were typically obtained for D_k/d_k from Eq. (10).

Each size distribution obtained by this technique was well approximated by a log-normal law, in accordance with literature results for sprays and other dispersions, and was little affected by the value chosen for the lightness threshold L_T.

The parameter MVD was used in this study as the characteristic diameter of the drops, since it is less sensitive than d_{32} to the exact details of the size distribution. The values measured by the above technique are reported in Fig. 5 as functions of Δp for all four nozzles. It can be observed that, for each nozzle, MVD decreases sharply as Δp rises from 0.2 to 0.5×10^6 N/m^2, but much less markedly for further increments of Δp. For comparison purposes, data from the manufacturer's data sheets are also reported. The results are in rough agreement with those provided by the manufacturer up to 0.8×10^6 N/m^2, but extend the data far beyond this limit.

3.3. Drop velocity

The drop velocity was determined by a photographic method, basically as in [19]. The spray issuing horizontally

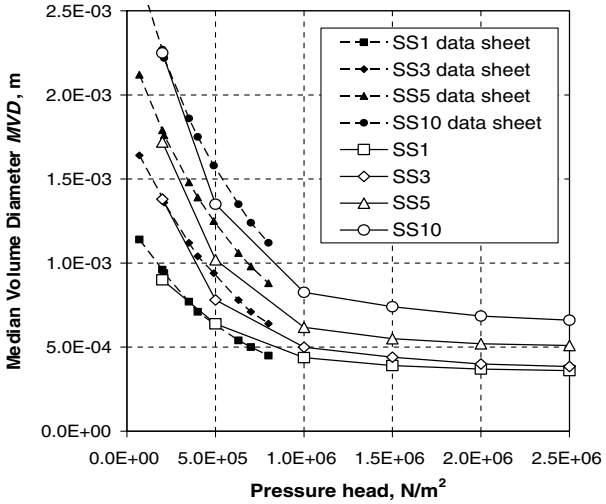

Fig. 5. Median volume diameter (MVD) determined by the impact method for $L = 0.2$ m as a function of the pressure head Δp for all four nozzles SS1 … SS10. Manufacturer's data in the range $0.1–0.8 \times 10^6$ N/m^2 are also shown.

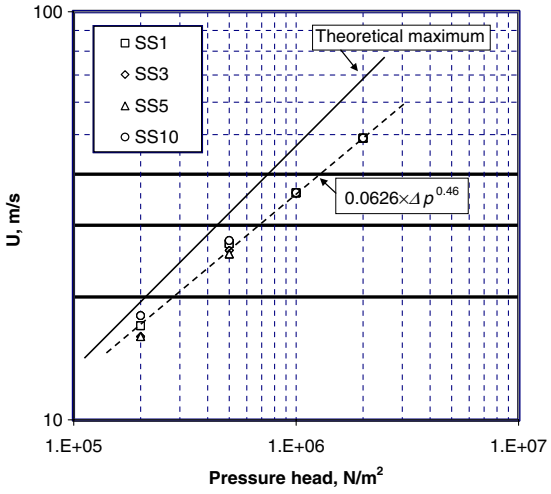

Fig. 6. Dependence of drop velocity on pressure head for all nozzle types. The solid line corresponds to the theoretical law $U = (2\Delta p/\rho)^{1/2}$, the broken line to a best fit of the experimental data.

from a single nozzle was illuminated from above by a light sheet, produced by a 500 W linear-bulb light source provided with an optical collimator (Pyrex© cylindrical lens and thin slit), and was photographed by a 6-Mpixel digital camera using shutter speeds between 1/1000 s and 1/250 s, according to the expected mean velocity, so as to obtain tracks between ~0.05 and ~0.10 m in real length. The image area was limited to within 0.1–0.2 m from the nozzle so as to reduce the component of the velocity dispersion which depends on the different drag deceleration experienced by drops of different size, see Section 1.2. A small amount of titanium dioxide powder was added to the water in order to make the tracks more easy to record photographically.

The resulting images were digitally enhanced by commercial image processing software in order to correct for the divergence of drop trajectories, increase contrast and reduce noise. In order to improve statistics, several such images were analyzed for each nozzle-Δp combination. Finally, the length of tracks was trivially converted into a velocity value since shutter speed, picture resolution and apparatus geometry were known. The result were histograms of velocity distribution which exhibited a roughly Gaussian behaviour; the corresponding modal value U was adopted as mean drop velocity for each nozzle and Δp.

The overall dependence of drop velocity on pressure head for all nozzle types is reported in Fig. 6. The solid line corresponds to the ideal law $U_{id} = (2\Delta p/\rho)^{1/2}$, i.e., to a 100% efficiency in the conversion of pressure into kinetic energy, while the broken line is a best fit of all available data. Needless to say, the above results are heavily affected by experimental uncertainties and can only be regarded as crude estimates of the drop speed, necessary to provide the internal variable U to be used in the heat transfer correlations.

4. Processing of temperature-time histories

The mid-plane temperature-time history during a hypothetical cooling test and the corresponding wall heat flux and wall temperature are schematically represented in Fig. 7a. The corresponding wall temperature–wall heat flux

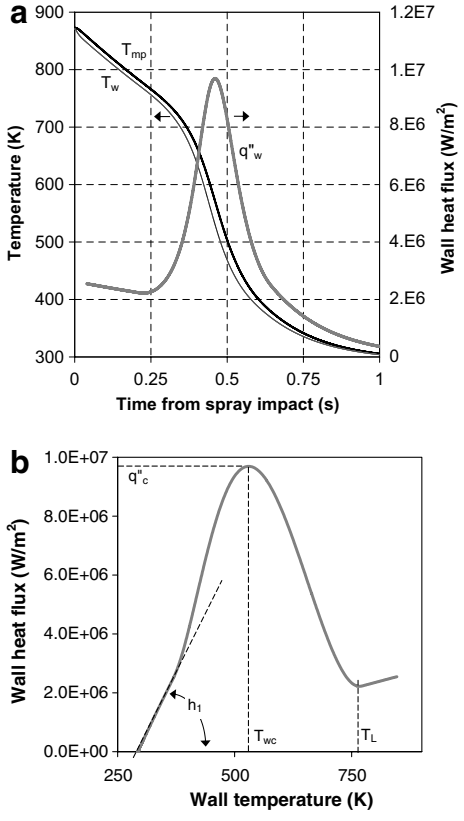

Fig. 7. (a) Cooling history: typical mid-plane temperature and corresponding wall temperature and wall heat flux. (b) Associated Nukiyama curve (arbitrary data).

relationship (Nukiyama curve) is shown in Fig. 7b. The data in Fig. 7 are arbitrary, and, for the sake of clarity, the transient is supposed to start from a sufficiently high temperature so that the Nukiyama curve exhibits all the possible features associated with different heat transfer regimes, including Leidenfrost point and film boiling heat transfer.

For vanishing Biot numbers $Bi = h\delta/k_{Al}$, the mid-plane and wall temperatures T_{mp}, T_w would coincide and a lumped parameter approach might be used. The wall heat flux q''_w would be proportional to (minus) the time derivative of T_{mp}, making the derivation of the various curves in Fig. 7 from the only one that is experimentally accessible, i.e., $T_{mp}(t)$, a trivial task.

For finite *Bi*, however, a more complex analysis is required; different ways of deriving the Nukiyama curve from experimental $T_{mp}(t)$ data will be discussed in detail in this Section.

4.1. First approach: solution of an inverse transient conduction problem

Once the thermal history $T_{mp}(t)$ at the target mid-plane during the rapid cooling stage has been recorded, an inverse heat conduction problem can be solved to compute wall temperature T_w and wall heat flux q''_w as functions of time. The choice of cooling the target by twin, opposite spray nozzles allows one to assume symmetry conditions throughout the transient, thus simplifying the mathematical treatment of the problem and making the thermal resistance between aluminium plates and thermocouples of little relevance since $\partial T/\partial x = 0$ in the mid-plane.

The inverse problem, like its direct counterpart, is governed by the one-dimensional (slab) transient heat conduction equation:

$$\rho c_p \frac{\partial T}{\partial t} = \frac{\partial}{\partial x} k \frac{\partial T}{\partial x} \tag{11}$$

in which x is the co-ordinate orthogonal to the slab and centred in its mid-plane; the subscript Al for aluminium was omitted in Eq. (11) since there is no ambiguity. However, in the inverse problem the initial condition $T(x, 0)$ and the inner solution $T_{mp}(t) = T(0,t)$ are known, and one has to determine the time dependent wall temperature $T_w(t) = T(\delta, t)$ and wall heat flux $q''_w(t) = -k(\partial T/\partial x)_{x=\delta}$, whereas in the direct problem the initial condition and a boundary condition of the mixed (Cauchy) type are known, and one has to determine the time dependent temperature profile $T(x,t)$.

Under the simplifying assumptions of uniform initial temperature distribution $T(x, 0) = T_0$ and constant physical properties of the slab (aluminium), an analytical solution to the above inverse problem was obtained by Stefan [24]. For the present symmetric configuration, it can be written as:

$$T_w = T_{mp}(t) + \frac{1}{2}\tau \frac{dT_{mp}}{dt} + \frac{1}{24}\tau^2 \frac{d^2 T_{mp}}{dt^2} + \dots \tag{12}$$

$$q''_w = -\frac{k}{\delta}\left[\tau \frac{dT_{mp}}{dt} + \frac{1}{6}\tau^2 \frac{d^2 T_{mp}}{dt^2} + \dots\right] \tag{13}$$

in which $\tau = \delta^2/\alpha$ is the conductive time constant of the slab, $\alpha = k/(\rho c_p)$ being the thermal diffusivity of the solid. The assumption of uniform initial temperature is well satisfied in the present tests. Further terms in the above series can be neglected with very little error.

The measured mid-plane temperature $T_{mp}(t)$ was inevitably affected by a variable amount of noise and irregularity, as shown by the symbols in Fig. 8 (which reports a short data sample from a test conducted with nozzle SS10, $\Delta p = 0.2 \times 10^6$ N/m^2 and $L = 0.2$ m). A first component of this, clearly recognizable in the figure, was due to electromagnetic interference by the 50 Hz grid frequency, and its entity exhibited the notorious unpredictable behaviour despite the efforts made to insulate target, thermocouples and wiring. A second component was due to the "granular" nature of the spray impact phenomenon; this was particularly significant at the lowest pressures and highest nozzle-target distances, when the number of drops hitting the target per unit time and unit area became relatively low.

As a consequence of the above irregularities, a preliminary filtering of the raw signal was found to be necessary before the derivatives in Eqs. (12) and (13) were numerically evaluated. Different alternative filters were tested and compared; the lines in Fig. 8 show the results of Gaussian filters having two different (half) widths of 5 and 20 $\times$ 10^{-3} s. In most cases, a half-width of 20 $\times$ 10^{-3} s was chosen as the best compromise between regularizing the data and preserving physically relevant information.

The mid-plane filtered temperature-time histories $T_{mp}(t)$ are reported in Fig. 9a for three experimental conditions

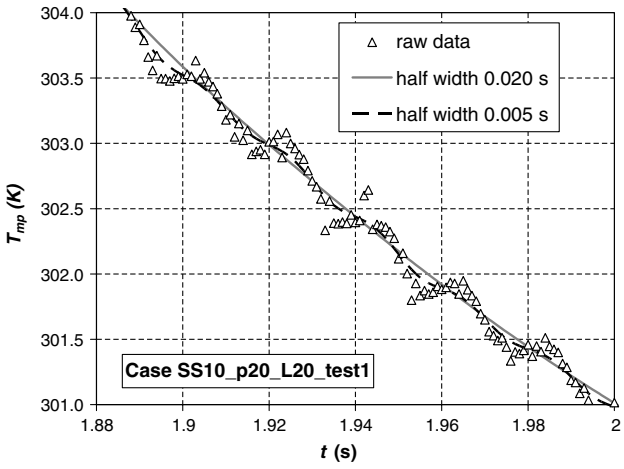

Fig. 8. Detail of a typical mid-plane temperature record: symbols: raw data; lines: data regularized by Gaussian filters with half-width 5 $\times$ 10^{-3} s (broken) or 20 $\times$ 10^{-3} s (solid). Interference by the 50 Hz (European) grid frequency can clearly be seen in the raw data.

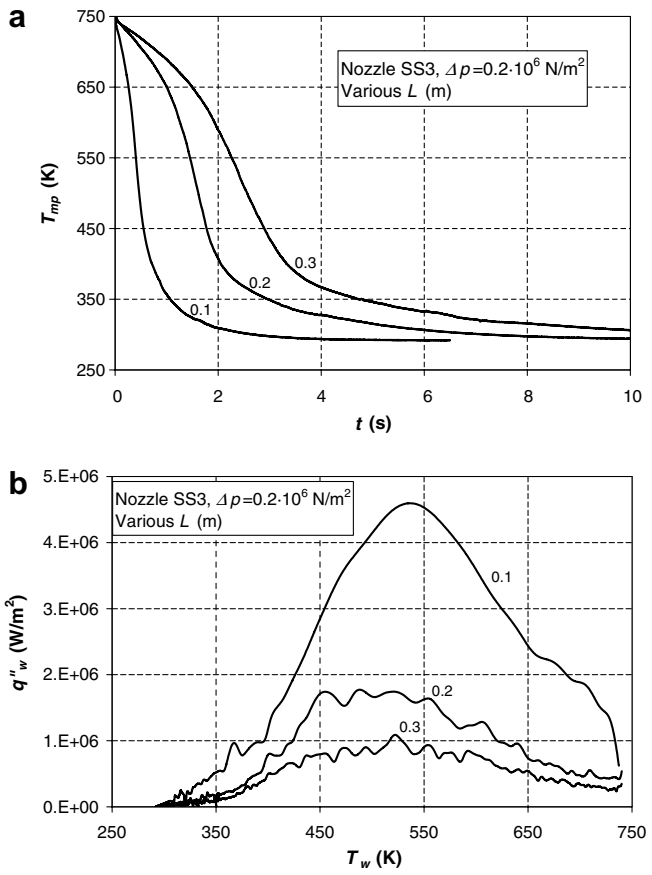

Fig. 9. Comparison of three test cases for nozzle SS3, $\Delta p = 0.2 \times 10^6$ N/m^2, $L = 0.1$, 0.2 and 0.3 m. (a) Mid-plane temperature histories; (b) corresponding heat transfer (Nukiyama) curves as obtained by solving the inverse conduction problem.

corresponding to nozzle SS3, $\Delta p = 0.2 \times 10^6$ N/m^2 and three values of the nozzle-target distance L (0.1, 0.2 and 0.3 m). Only the first 10 s of the transients are shown; the target attained practical thermal equilibrium with the fluid after a time varying between 5 and 20 s according to the value of L. As expected, smaller distances yielded faster cooling transients; cooling rates up to 1500 K/s were observed between ~600 and ~500 K for $L = 0.1$ m. Note that the increase of L causes mainly a decrease in G without directly affecting U and MVD (although minor differences may arise from the braking and filtering effects discussed in Section 1.2).

By reporting $q''_w(t)$ as a function of $T_w(t)$, the Nukiyama curves reported in Fig. 9b are obtained. These show that the critical heat flux increases from $\sim 1 \times 10^6$ W/m^2 at 0.3 m to $\sim 4.5 \times 10^6$ W/m^2 at 0.1 m, while the DNB temperature T_c at which it is attained varies little and is ~520 K at all distances. The single-phase heat transfer coefficient, estimated as indicated in Fig. 7b, varies between ~1500 W/(m^2 K) at 0.3 m to ~8500 W/(m^2 K) at 0.1 m. Some indications of the presence of a Leidenfrost transition (at ~720 K) are exhibited only by the curves obtained for the larger distances, but not by the curve for $L = 0.1$ m. This suggests that, under the corresponding test conditions, the Leidenfrost temperature T_L is above the maximum wall temperature attained in the tests (~750 K).

For the case at $L = 0.1$ m, significant differences (up to ~30 K) are observed between T_{mp} and T_w. This is coherent with the fact that for this case the maximum Biot number, computed as $(q''_c/(T_c - T_f)) \times \delta/k$, is ~0.16, a relatively high value for which the lumped parameter approach is not justified. Smaller, but still significant, differences exist for the cases characterized by a slower cooling.

The degree of repeatability typically exhibited by the results is illustrated in Fig. 10, which reports the boiling curves obtained in three different tests for nozzle SS3, $\Delta p = 0.2 \times 10^6$ N/m^2 and $L = 0.3$ m. For these latter tests, characterized by a low numerical rate of drops impinging the target, statistical fluctuations in the temperature data are not sufficiently removed by the Gaussian filter even by using a half width a of 0.1 s, and cause the curves to exhibit considerable irregularities. Under these conditions, the repeatability of the results can be asserted only in a statistical sense, and the derivation of important heat transfer parameters such as the single-phase heat transfer coefficient h_l and the critical heat flux q''_c, from the irregular boiling curves involves some considerable amount of subjective judgment.

4.2. Second approach: solution of a direct transient conduction problem and optimization of the boiling curve parameters

An alternative approach relies on the observation that, if the boiling curve were known in the form of a functional relationship between the wall heat flux and the wall temperature,

$$q''_w = f(T_w) \tag{14}$$

then the whole transient solution $T(x,t)$ – and, in particular, the mid-plane temperature $T_{mp}(t) = T(0,\ t)$ – might

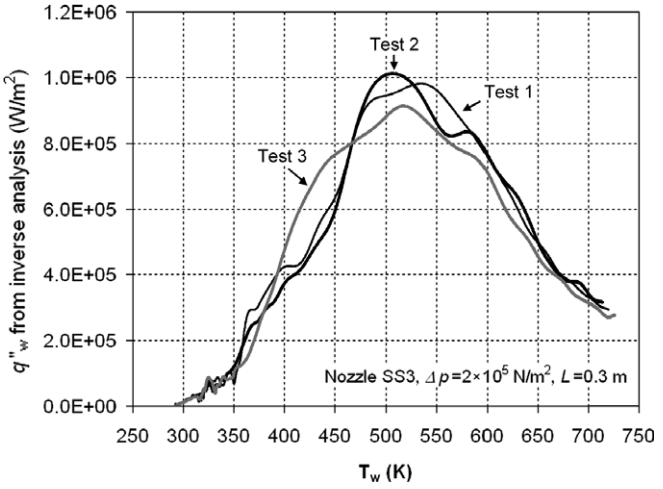

Fig. 10. Repeatability of the results: heat transfer curves obtained by the inverse analysis method in three different tests for nozzle SS3, $\Delta p = 0.2 \times 10^6$ N/m^2, $L = 0.3$ m.

be computed by solving the transient heat conduction Eq. (11) with the known initial condition of uniform temperature T_0.

For an arbitrary choice of the functional dependence f in Eq. (14), the computed mid-plane temperature, say $T^*_{mp}(t)$, will differ from its experimental counterpart $T_{mp}(t)$; the discrepancy can be measured, for example, by the root mean square error E:

$$E = \sqrt{\frac{1}{n-1}\sum_{k=1}^{n}\left[T_{mp}(t_k) - T^*_{mp}(t_k)\right]^2} \tag{15}$$

in which t_k is the time of the generic kth measurement and n is the total number of experimental points. Now, the "true" boiling curve can be determined, in principle, by solving a variational problem: find the function f that minimizes the functional E.

In order practically to solve the above problem, the form of the functional dependence f has to be prescribed by a finite (and, possibly, small) number m of parameters c_j so that E becomes a function of $c_1 \ldots c_m$ and the problem is reduced to that of finding the minimum of the function $E(c_1 \ldots c_m)$. Different parametrical descriptions of the boiling curve were tested; in the end, that represented in Fig. 11 was chosen as a compromise between generality and simplicity.

It assumes that, for low wall temperatures, heat transfer is governed by Newton's law with a single-phase (liquid) heat transfer coefficient h_1, whereas post-critical heat transfer is governed by a similar law with a lower single-phase (vapor) coefficient h_2. The intermediate region (nucleate and transitional boiling) is described by a fifth-order polynomial $b_0 + b_1 T_w + b_2 T_w^2 + b_3 T_w^3 + b_4 T_w^4 + b_5 T_w^5$ which exhibits a maximum q''_c (critical heat flux) at a wall temperature T_c. Coincidence in value and derivative between the polynomial and the two straight lines is imposed at points 1 and 2.

The resulting curve (thick line in Fig. 11) is uniquely described by the six parameters $c_i = (T_1, h_1, T_2, h_2, T_c, q''_c)$. The coefficients b_k are computed from these by imposing value and derivative of q''_w at points 1, 2, c. Note that point 2 is close to, but not strictly coincident with, the Leidenfrost point as it is usually defined (relative minimum of the boiling curve).

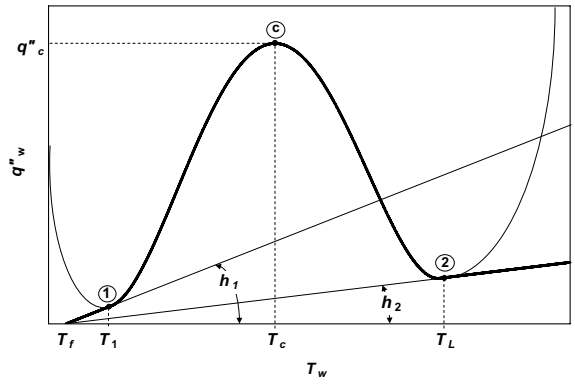

Fig. 11. Parameterization of the boiling curve.

For each set of parameters, the direct transient heat conduction problem described by Eq. (11) with the boundary condition $q''_w = -k(\partial T/\partial x)_{x=\delta} = f[T(\delta, t)]$ and initial condition $T(x, 0) = T_0$ was solved by a simple finite difference method with explicit time stepping. Details are standard and will not be reported here. A sensitivity study was conducted by comparing the results with the analytical slab solution [25] for the simple case of constant physical properties and constant h, when the boundary condition reduces to the Cauchy one $q''_w = -k(\partial T/\partial x)_{x=\delta} h[T(\delta, t) - T_f]$. This showed that using 20 grid nodes along x ($\Delta x = \delta/20$) and a time step Δt of 5×10^{-5} s (satisfying the diffusive stability criterion $\Delta t < \Delta x^2/\alpha$) provided sufficient grid- and time step-independence for the present purposes.

In solving the direct problem, no simplifying assumption was made concerning the relevant physical properties of aluminium (in particular, thermal conductivity k and thermal diffusivity α), which were allowed to vary with the temperature [22]. Comparative simulations showed that the variation of the physical properties *does* have a significant influence on the cooling transients. Therefore, the possibility of taking full account of variable physical properties is a clear advantage of the "direct" method on the "inverse" one discussed in above.

In order to solve the minimum (optimization) problem discussed above, several alternative algorithms were implemented and tested [26]. They all amount to moving the point P representative of the Nukiyama curve stepwise in the six-dimensional space of the parameters c_j by some strategy until a minimum of the error E is obtained. For example, in the Conjugate Gradient (CG) method, at each step the six partial derivatives are numerically evaluated by giving each variable a small variation in both directions, and the direction of the gradient ∇E is determined. The point P of co-ordinates c_j in parameter space is then moved in steps along the direction opposite to the gradient until no further reduction is observed. ∇E is now re-computed and a new cycle begins. The step size is reduced as the computation progresses. The method is fast in its initial stages, but, due to the numerical approximations involved in the computation of E and of its derivatives, fails in the proximity of the minimum, when these latter become very small. Therefore, it was implemented in a modified form in which, when a displacement in the direction opposite to the computed gradient yields no reduction in E, it is replaced by a random jump using a pseudo-random number generator.

The boiling curve predicted by the direct method with the CG algorithm for the case of nozzle SS3, $\Delta p = 0.2 \times 10^6$ N/m^2, $L = 0.3$ m, test 1 is compared in Fig. 12a with that obtained by using the inverse technique (also reported in Fig. 10). It can be observed that the main features, such as the maximum heat flux and the slope in the single-phase region, are roughly equivalent, but, of course, only the direct method yields a smooth curve. Note that it also predicts the existence of a heat transfer minimum (Leidenfrost

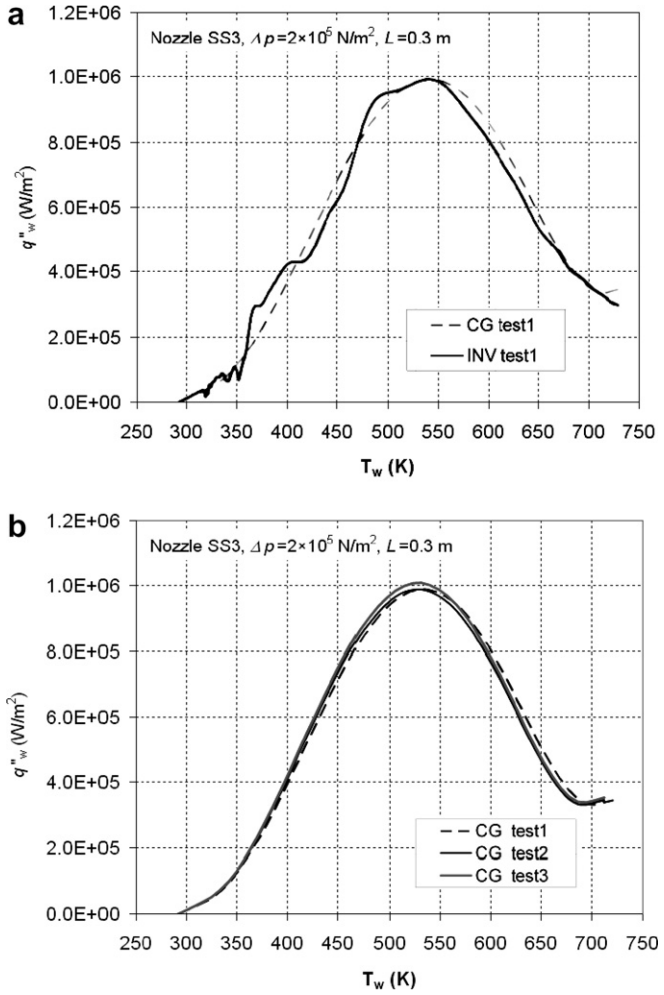

Fig. 12. Results of the optimization technique for case SS3, $\Delta p = 0.2 \times 10^6$ N/m^2, $L = 0.3$ m. (a) Comparison between boiling curves obtained for test 1 using the inverse method (INV) and the direct method with the CG optimization algorithm. (b) Boiling curves obtained by the direct method for tests 1, 2 and 3.

point) at $T_w \approx 700$ K, not shown by the inverse technique. Since this temperature is close to the maximum temperature attained in the test (~720 K), the Leidenfrost point can only be inferred from the optimization process but can *not* be regarded as direct experimental evidence.

For the same experimental conditions, Fig. 12b compares the boiling curves obtained by processing the data from tests 1, 2 and 3 by the *E*-minimization method and the CG algorithm. It should be compared with Fig. 10: here the three curves are basically identical, whereas those in Fig. 10, obtained by the inverse technique, exhibit obvious and irregular differences.

4.3. Comparison of the inverse and direct methods

Each of the two methods described above for deriving the Nukiyama curve from "raw" temperature data has its own merits and demerits. The advantages of the "direct" method over the "inverse" one can be summarized as follows:

- It relies much less on the regularity of the experimental data: no filtering is required, temperature-time histories affected by significant, but localized, lacks or discontinuities can be effectively processed, and repeated tests conducted under the same experimental conditions result in basically identical boiling curves.
- It allows the objective (human-independent) quantitative assessment of relevant features of the boiling curves, such as the single-phase heat transfer coefficient h_1 and the maximum, or critical, heat flux q''_c.
- It takes full account of the temperature dependence of the physical properties of the target.

On the other hand, the "inverse" method presents its own points of strength:

- No "a priori" shape of the boiling curve has to be assumed, which allows for a greater flexibility of application. In particular, the method can be extended to the processing of data obtained under different cooling conditions, when the physics of the phenomenon may not be known in advance.
- The numerical processing required – including data filtering – is relatively simple, and was actually implemented in a spreadsheet in the present work.

In the end, the choice of the method to be adopted will depend on the quality of the available data and on the degree to which the physics of the phenomenon under investigation are known in advance. In the following Section, only results obtained by the direct method will be considered since quantitative correlations, exempt from subjective bias, will be sought.

5. Results and proposed correlations

5.1. Summary of the experimental results

Table 2 summarizes the 64 operating conditions for which cooling tests were conducted and the most relevant of the corresponding results.

The experimental conditions are indicated in columns 2 to 4 and include all combinations of the following values of the external (control) parameters SS, Δp, L:

- nozzle type SS = SS1–SS3–SS5–SS10;
- pressure head $\Delta p = 0.2$–0.5–1–2×10^6 N/m^2;
- nozzle-target distance $L = 0.1$–0.2–0.3–0.4 m.

For each experimental condition, the internal (local) parameters G, MVD, U, as determined by the methods discussed in Section 3, are indicated in columns 5–7; they varied in the following range:

- specific mass flow rate $G = 0.33$–32.7 kg/(m^2 s);
- median volume diameter MVD $= 0.37$–2.25×10^{-3} m;
- modal velocity $U = 17.2$–49.6 m/s.

Table 2
Summary of test cases and results obtained in the present work

Case	Nozzle	Δp, 10^6 N/m^2	L, m	G, kg/(m^2 s)	MVD, 10^{-3} m	U, m/s	h_l, W/(m^2 K)	q_c, 10^6 W/m^2
1	SS1	0.2	0.1	2.15	0.9	17.2	2902	2.370
2	SS1	0.2	0.2	0.85	0.9	17.2	2035	1.711
3	SS1	0.2	0.3	0.44	0.9	17.2	1499	1.101
4	SS1	0.2	0.4	0.33	0.9	17.2	1045	0.510
5	SS1	0.5	0.1	2.51	0.639	26.2	4985	2.971
6	SS1	0.5	0.2	0.87	0.639	26.2	2315	1.778
7	SS1	0.5	0.3	0.45	0.639	26.2	1305	1.103
8	SS1	0.5	0.4	0.33	0.639	26.2	1053	0.676
9	SS1	1	0.1	3.55	0.437	36.1	6345	3.196
10	SS1	1	0.2	1.23	0.437	36.1	3860	2.729
11	SS1	1	0.3	0.62	0.437	36.1	2843	1.279
12	SS1	1	0.4	0.44	0.437	36.1	2000	1.237
13	SS1	2	0.1	5.2	0.37	49.6	10,102	4.918
14	SS1	2	0.2	1.84	0.37	49.6	4906	3.158
15	SS1	2	0.3	1.03	0.37	49.6	3355	2.006
16	SS1	2	0.4	0.72	0.37	49.6	2200	1.500
17	SS3	0.2	0.1	3.6	1.38	17.2	6406	3.424
18	SS3	0.2	0.2	1.1	1.38	17.2	2824	2.118
19	SS3	0.2	0.3	0.7	1.38	17.2	1590	1.128
20	SS3	0.2	0.4	0.45	1.38	17.2	1093	0.687
21	SS3	0.5	0.1	4.72	0.781	26.2	9095	3.300
22	SS3	0.5	0.2	1.71	0.781	26.2	4101	2.607
23	SS3	0.5	0.3	1	0.781	26.2	2735	1.860
24	SS3	0.5	0.4	0.61	0.781	26.2	1405	1.101
25	SS3	1	0.1	6.66	0.499	36.1	11,759	3.958
26	SS3	1	0.2	2.25	0.499	36.1	4556	2.591
27	SS3	1	0.3	1.25	0.499	36.1	2998	1.973
28	SS3	1	0.4	0.91	0.499	36.1	2658	1.425
29	SS3	2	0.1	9.6	0.4	49.6	14,622	6.607
30	SS3	2	0.2	3.3	0.4	49.6	7933	4.045
31	SS3	2	0.3	2.01	0.4	49.6	6184	3.168
32	SS3	2	0.4	1.51	0.4	49.6	4820	2.353
33	SS5	0.2	0.1	5.79	1.72	17.2	10,435	4.995
34	SS5	0.2	0.2	2.15	1.72	17.2	4528	2.913
35	SS5	0.2	0.3	1.24	1.72	17.2	2071	1.799
36	SS5	0.2	0.4	0.82	1.72	17.2	1090	1.200
37	SS5	0.5	0.1	7.96	1.02	26.2	11,260	4.593
38	SS5	0.5	0.2	2.89	1.02	26.2	6578	3.330
39	SS5	0.5	0.3	1.57	1.02	26.2	3800	2.200
40	SS5	0.5	0.4	1	1.02	26.2	2400	1.650
41	SS5	1	0.1	10.66	0.618	36.1	12,506	6.731
42	SS5	1	0.2	3.43	0.618	36.1	7327	3.648
43	SS5	1	0.3	1.86	0.618	36.1	5933	2.831
44	SS5	1	0.4	1.23	0.618	36.1	3823	2.208
45	SS5	2	0.1	16.53	0.52	49.6	20,483	8.680
46	SS5	2	0.2	5.22	0.52	49.6	10,388	4.892
47	SS5	2	0.3	3.01	0.52	49.6	8406	3.755
48	SS5	2	0.4	2.11	0.52	49.6	6435	3.086
49	SS10	0.2	0.1	9.16	2.25	17.2	8682	6.081
50	SS10	0.2	0.2	3.48	2.25	17.2	5342	2.674
51	SS10	0.2	0.3	1.96	2.25	17.2	2789	1.588
52	SS10	0.2	0.4	1.21	2.25	17.2	1350	1.200
53	SS10	0.5	0.1	13.75	1.35	26.2	19,024	9.000
54	SS10	0.5	0.2	4.53	1.35	26.2	8862	4.556
55	SS10	0.5	0.3	2.47	1.35	26.2	4503	2.530
56	SS10	0.5	0.4	1.57	1.35	26.2	2507	1.800
57	SS10	1	0.1	20.88	0.826	36.1	30,320	10.500
58	SS10	1	0.2	6.01	0.826	36.1	12,195	5.624
59	SS10	1	0.3	3.05	0.826	36.1	6048	3.530
60	SS10	1	0.4	2.14	0.826	36.1	3902	2.520
61	SS10	2	0.1	32.72	0.685	49.6	27,720	11.270
62	SS10	2	0.2	9.41	0.685	49.6	15,260	7.135
63	SS10	2	0.3	5.57	0.685	49.6	9597	5.564
64	SS10	2	0.4	3.52	0.685	49.6	6501	4.200

Table 3
Summary of test cases and results obtained in previous work (Ciofalo et al. 1999)

Case	Nozzle	Δp, 10^6 N/m^2	L, m	G, kg/(m^2 s)	MVD, 10^{-3} m	U, m/s	h_1, W/(m^2 K)	q_c, 10^6 W/m^2
65	TG1	0.2	0.05	9	0.96	12.7	13,000	4.600
66	TG1	0.4	0.05	10	0.71	19.5	20,000	7.050
67	TG1	0.8	0.05	12	0.45	26.0	30,000	9.400
68	TG2	0.2	0.05	20.5	1.39	13.9	25,000	7.050
69	TG2	0.4	0.05	24.5	1.04	19.0	39,000	8.500
70	TG2	0.8	0.05	30	0.64	28.2	55,000	9.400
71	TG5	0.2	0.05	27.5	1.79	12.6	31,000	5.950
72	TG5	0.4	0.05	34.5	1.39	19.0	50,000	8.050
73	TG5	0.8	0.05	44.5	0.88	26.1	80,000	10.850
74	TG10	0.2	0.05	49	2.27	12.6	50,000	10.000
75	TG10	0.4	0.05	59	1.75	18.5	76,000	10.950
76	TG10	0.8	0.05	81.5	1.12	24.0	121,000	12.000

As mentioned above, for each condition a minimum of three valid tests were conducted, and the corresponding values of h_1 and q_c'' were averaged. Therefore, the present data required 192 valid individual cooling tests. Results are reported in columns 8 and 9; they are all based on the "direct" (minimum search) approach discussed in Section 4.2, i.e., they represent optimum values of two of the six parameters that characterize the parameterized Nukiyama curve in Fig. 11. The remaining parameters, i.e. the single phase – boiling transition temperature T_1, the DNB temperature T_c, and the quantities T_2, h_2 characterizing the (hypothetical) Leidenfrost point exhibited a random variability, correlated poorly with the "internal" spray variables and are not reported in the present study.

For comparison purposes, Table 3 reports the same above quantities for the tests conducted in the previous study [19]. As mentioned earlier, they were characterized by a fixed nozzle-target distance of 5×10^{-2} m, pressure heads in the range 0.2–0.8 $\times 10^6$ N/m^2, and 4 types of nozzles (TG1–TG2–TG5–TG10) similar, but not identical, to those utilized in the present study.

It should be observed that, although most data correlation studies make ample use of dimensionless numbers, this method was not followed here. In fact, the authors feel that, in experiences conducted for a single working fluid (water); for a practically constant initial temperature T_f (which was ~296 K in all tests); for a single hot wall composition and surface finish; and for a narrow range of some of the other parameters, such as the drop speed (which varied only between 17 and 50 m/s), the use of dimensionless groups such as *We* or *Re* would contribute little to the generality of the results and might even be misleading, conveying the impression of a universality which would not really be there.

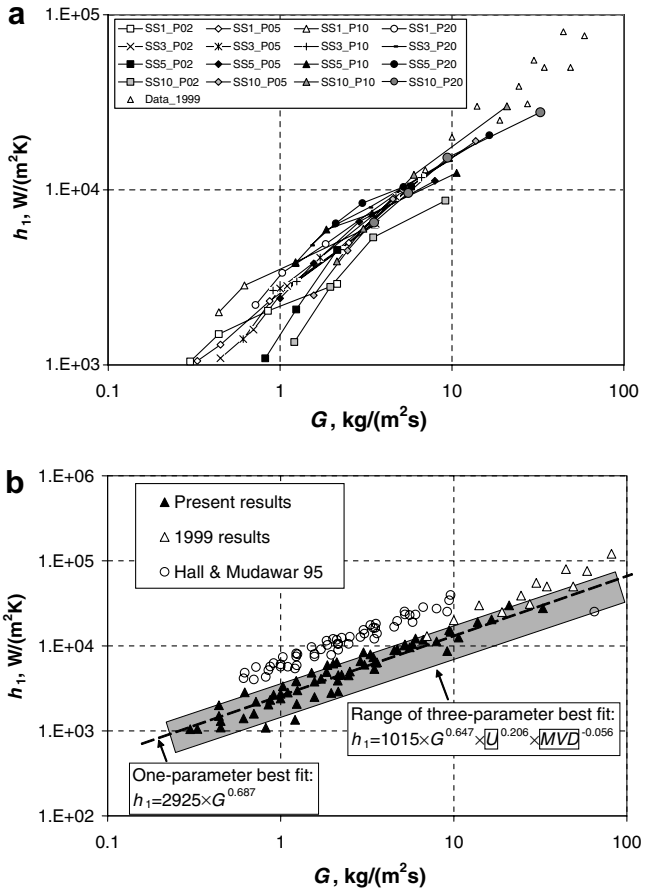

Fig. 13. Single-phase heat transfer coefficient h_1 as a function of the specific mass flow rate G. (a) Results reported by series differing in nozzle (SS) and Δp. (b) Results compared with one-parameter and three-parameter best-fit power law correlations. Results by Hall and Mudawar [1] are also shown.

5.2. Correlation of the single-phase heat transfer coefficient, h_1

Fig. 13 reports the single-phase heat transfer coefficient h_1, defined as parameter c_2 in the "direct" minimum search (optimization) approach of Section 4.2, for cases 1–64 as a function of the specific mass flow rate G. Results from the previous study [19] are also reported for comparison purposes. For clarity purposes, the figure was split into two graphs as discussed here below.

In Fig. 13a, the present results are grouped by series, differing by nozzle type (SS) and pressure head (Δp). Within each series, data points are connected by a line and differ only by the nozzle-target distance L, which affects mainly

the specific mass flow rate G while its effect on MVD and U are small and indirect (and, however, were not taken into account in the hydrodynamic characterization study). It can be observed that the different data series fall within a relatively narrow dispersion band and do not exhibit any obvious discontinuity, which suggests that the influence of the parameters depending on nozzle type and pressure head, MVD and U, is only secondary with respect to the dependence upon G.

In Fig. 13b, the present results are shown as scattered data points (solid triangles) and are compared with different correlations. Results from [19] are also reported (hollow traingles), but were *not* used in the derivation of best-fit correlations discussed below; it should be observed that, unlike the present ones, they were estimated manually from Nukiyama curves derived by the "inverse" approach described in Section 4.1.

The present data are fairly well approximated by a least-squares best-fit power law which correlates them with the specific mass flow rate G alone, and is reported on the graph as a broken line:

$$h_1 = 2925 \times G^{0.687} \tag{16}$$

in which h_1 is expressed in W/(m^2 K) and G in kg/(m^2 s). The rms error of Eq. (16), as computed over the present 64 experimental points, is ~1523 W/(m^2 K). It can be seen that also the data from [19] are not far from following the same power law, although, as was observed above, they were *not* taken into account in deriving it.

A more complete analysis, correlating h_1 with all three variables ($G, U,$ MVD) which were assumed to affect heat transfer in this study, yields the following least squares best fit:

$$h_1 = 1015 G^{0.647} U^{0.206} \mathrm{MVD}^{-0.056} \tag{17}$$

(U in m/s, MVD in m), with a rms error of ~1489 W/(m^2 K). Thus, taking also the residual dependence of h_1 on drop velocity and diameter into account does not significantly improve the quality of the correlation, yields low power law exponents for U and MVD, and affects only slightly the exponent in the power law dependence upon G, as compared with the univariate correlation (18). The diameter dependence, in particular, is well within the range of the experimental uncertainties and does not possess a reliable physical significance. Eq. (17) is also reported in Fig. 13b, where it translates into a scatter band rather than into a single line due to the dependence on U and MVD, which are not represented in the graph.

Predictions obtained by applying the Hall and Mudawar [1] correlation for h_1, Eq. (8), to the present values of G and MVD are also reported in Fig. 13b for comparison purposes (hollow circles) in the validity range $G = 0.58$–10 kg/(m^2 s) of their study. The assumption $d_{32} = 0.8$ MVD was used. The correlation by Hall and Mudawar gives a large and systematic overprediction (by a factor of ~2) with respect to the present results. A possible explanation for, at least, part of this discrepancy is that the single-phase heat transfer coefficient measured by Hall and Mudawar was an average in the single-phase convection range, while the quantity h_1 as defined here is rather the angular coefficient of the "best" straight line fitting the Nukiyama curve in some low T_w range. A further discrepancy is that, unlike the present experimental results and Eq. (17), the Hall and Mudawar correlation does not contain any explicit dependence of h_1 on the drop velocity, while expressing a significant dependence on the drop diameter.

5.3. Correlation of the critical heat flux, q''_c

Fig. 14 reports the critical heat flux q''_c, defined as parameter c_6 in the "direct" minimum search (optimization) approach of Section 4.2, for cases 1–64 as a function of the specific mass flow rate G. As in the case of h_1, results from the previous study are also reported for comparison purposes. For clarity purposes, the figure is split into two different graphs as the previous one.

In Fig. 14a, the present results are grouped by series, differing by nozzle type (SS) and pressure head (Δp). Within

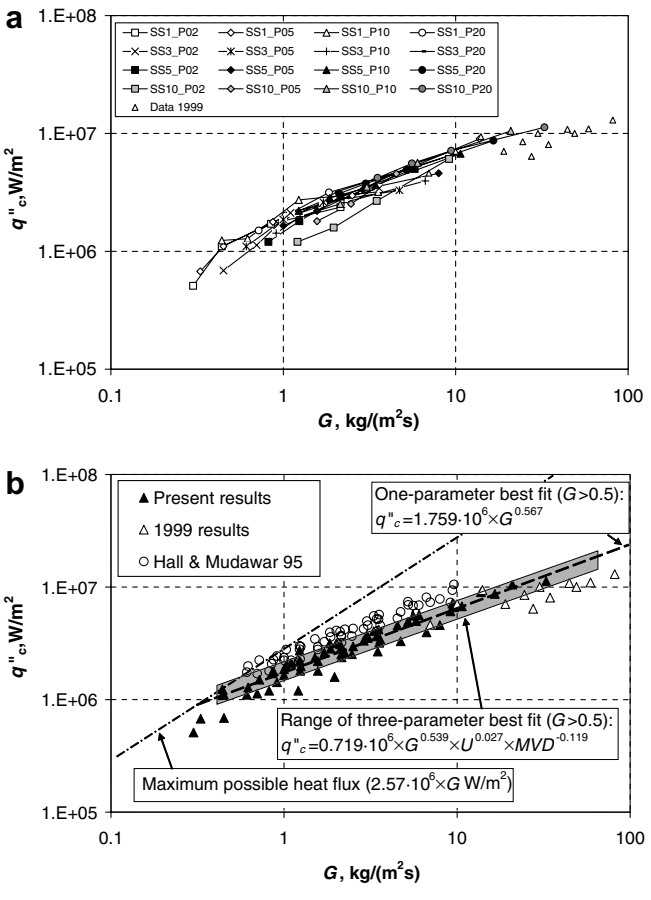

Fig. 14. Critical heat flux q''_c as a function of the specific mass flow rate G. (a) Results reported by series differing in nozzle (SS) and Δp. (b) Results compared with one-parameter and three-parameter best-fit power law correlations for $G > 0.5$ kg/(m^2 s). The dash-dot line is the maximum heat flux, $(c_p(T_{sat} - T_f) + J_{fg})G$. Results by Hall and Mudawar [1] are also shown.

each series, data points are connected by a line and differ only by the nozzle-target distance L, which can be supposed to affect only the specific mass flow rate G but not MVD and U. As in the case of the single-phase heat transfer coefficient, the different data series fall within a relatively narrow dispersion band and do not exhibit any obvious discontinuity, suggesting that the influence of the parameters depending on nozzle type and pressure head, MVD and U, is secondary with respect to the dependence upon G.

In Fig. 14b, the present results are reported together as scattered solid triangles and are compared with various correlations and limit lines. Data from the 1999 study are also shown (hollow triangles), but were *not* used in the following data correlation. The present data exhibit a clear change of slope in the proximity of $G = 0.5$ kg/(m^2 s), which is well explained by taking account of the maximum heat flux that can be removed under steady-state conditions from the hot wall:

$$q''_{\max} = [c_p(T_{\text{sat}} - T_{\text{f}}) + J_{fg}]G \tag{18}$$

in which $T_{\text{sat}} = 373.15$ K in all the present tests. Eq. (18) is represented in Fig. 14b by a dash-dot line; it is clear that, at low G, the maximum flux is closely approached by some of the experimental points, whereas, at larger G, the results follow a different trend.

This observation suggests that a power-law correlation can be sought only for those results which fall sufficiently far from the maximum heat flux line, i.e., in the present case, for the specific mass flow rate range $G > 0.5$ kg/(m^2 s). In this region, the present results are fairly well approximated by the univariate best-fit power law correlation:

$$q''_{\text{c}} = 1.759 \times 10^6 G^{0.567} \tag{19}$$

with a rms error, computed over the present experimental points for which $G > 0.5$ kg/(m^2 s), of 5.43×10^5 W/m^2. Eq. (19) is represented in Fig. 14b by a broken line. The data from [19] tend to fall below this correlation line.

A more complete analysis, correlating q''_{c} with all three parameters which were assumed to affect heat transfer in this study, yielded the following least squares best-fit power law:

$$q''_{\text{c}} = 0.719 \times 10^6 G^{0.539} U^{0.027} \text{MVD}^{-0.119} \tag{20}$$

(U in m/s, MVD in m), with a rms error of 5.40×10^5 W/(m^2 K). Thus, as in the case of the single phase heat transfer coefficient discussed above, taking the dependence of q''_{c} on drop velocity and diameter into account does not significantly improve the quality of the best fit, yields small power law exponents for U and MVD, and does not significantly affect the exponent in the power law dependence upon G with respect to the univariate correlation (19). The velocity dependence, in particular, is well within the range of the experimental uncertainties and probably does not have any physical significance. Eq. (20) is also reported in Fig. 14b, where it translates into a scatter band rather than into a single line due to the dependence on U and MVD.

Finally, predictions obtained by applying the Hall and Mudawar [1] correlation for q''_{c}, Eq. (9), to the present values of G and MVD are also reported in Fig. 14b for comparison purposes (hollow circles) in the validity range $G = 0.58$–10 kg/(m^2 s) of their study. Eq. (9) was applied using the assumption $d_{32} = 0.8$ MVD. It gives a fair agreement with the present results, with a moderate overprediction of q''_{c}; as compared with Eq. (20), it predicts a slightly higher exponent for G (0.604 instead of 0.537) and a slightly stronger dependence on MVD (exponent -0.198 instead of -0.120), while it basically agrees with the present results in predicting the absence of an independent effect of the drop velocity U (exponent 0 instead of 0.027). On the basis of Fig. 14b, it can be argued that the power laws obtained for $G < 10$ kg/(m^2 s) can *not* be extrapolated to higher specific mass flow rates, for which a lower exponent seems to be more adequate. This reflects the fact that the efficiency by which heat is removed from the hot wall in the nucleate boiling regime falls as the mass flow rate increases, probably in correspondence with an increased bouncing of the drops and/or of the liquid film formed on the surface.

Correlations (19) or (20) should be used only as far as they yield values of q''_{c} smaller than the maximum heat flux $q''_{\max}$ in Eq. (18). This latter should be used in all other cases, although more as a limiting line than as a predictive law. Note that, in principle, in *transient* cooling tests the heat flux may even exceed $q''_{\max}$ when transition from film to wetting (nucleate) boiling occurs and the water layer adhering to the target during the film boiling phase is abruptly vaporized.

An interesting implication of the different power laws by which the critical heat flux q''_{c} and the single-phase heat transfer coefficient h_1 vary with G is that, as G increases, single-phase heat transfer rates (portion of the heat transfer

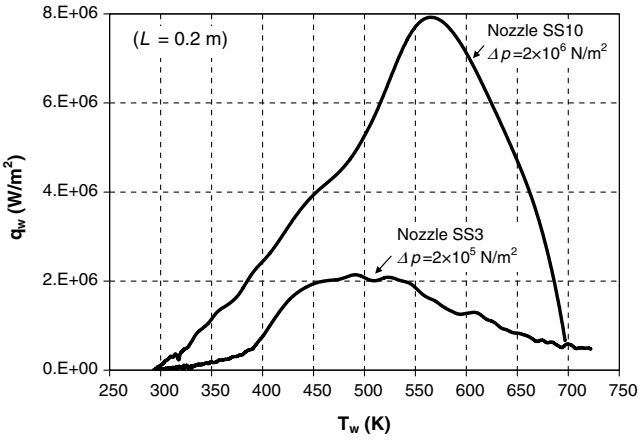

Fig. 15. Comparison of heat transfer curves obtained at $L = 0.2$ m for high G (nozzle SS10, $\Delta p = 2 \times 10^6$ N/m^2) and low G (nozzle SS3, $\Delta p = 0.2 \times 10^6$ N/m^2), showing the different relative importance of convection and boiling.

curve below $T_w = 373$ K) increase more rapidly than the critical heat flux (maximum region of the heat transfer curve), so that the relative importance of single-phase convection increases with respect to boiling. As a consequence, heat transfer curves obtained for low values of G exhibit a "knee" in the proximity of $T_w = 373$ K which is absent in the case of high G (Fig. 15).

6. Conclusions

The present study extended a previous investigation on spray cooling [19], in which only temperatures up to 570 K could be attained and the nozzle-target distance was fixed.

A new experimental rig allowed different nozzle types (SS), pressure heads Δp (up to 2×10^6 N/m^2) and nozzle-target distances L (from 0.1 to 0.4 m) to be investigated. The initial target temperatures could be raised up to 750 K. The accuracy of temperature measurements was improved by using a 16-bit, high-frequency A/D converter.

A preliminary characterization study provided the dependence of the *internal* parameters G (specific mass flow rate), U (mean drop velocity) and MVD (median volume diameter of the drops) upon the above *external* parameters SS, Δp, L. Only G could be determined with good accuracy, whereas measurements of U and MVD were much more crude; however, due to the weak dependence of heat transfer rates on these latter quantities, this was not regarded as a major shortcoming.

Heat transfer (Nukiyama) curves were obtained for a variety of nozzles and operating conditions by post-processing time histories of the target's mid-plane temperature. Two alternative methods were used, the first based on the solution of an inverse transient conduction problem and the second on the optimization of a parameterized Nukiyama curve. This latter was selected as the more reliable and human-independent of the two techniques.

The critical heat flux q''_c and the single-phase heat transfer coefficient h_1 were obtained from the heat transfer curves. They were expressed in the form $q''_c = q''_c(G, U, \mathrm{MVD})$ and $h_1 = h_1(G, U, \mathrm{MVD})$. A correlation analysis showed that both q''_c and h_1 were mainly affected by the specific mass flow rate G, while the remaining parameters (U, MVD) played only a secondary role. The other quantities characterizing the Nukiyama curve correlated poorly with the above "internal" parameters; in particular, reliable estimates of the Leidenfrost temperature and of the corresponding heat flux, or heat transfer coefficient, could not be obtained due to the limitations in the maximum test temperature ($\sim$750 K).

Once expressed as a function of G only, the single-phase heat transfer coefficient h_1 was found to increase as $G^{0.687}$ over the whole range of experimental conditions, in agreement with the 2/3 power law commonly reported for impinging jets and flows with reattachment. Including the variables U and MVD in the analysis did not improve to a significant extent the quality of the correlation.

As regards the critical heat flux q''_c, this quantity followed fairly well a $G^{0.567}$ power law in the intermediate mass flow rate range $G = 0.5$–10 kg/(m^2 s). For lower mass flow rates the measured values of this quantity fell below the limiting line $q''_{max} = [c_p(T_{sat} - T_f) + J_{fg}]G$, as dictated by physical reasons, while at the highest flow rates the available data suggest that the G exponent decreases as the efficiency of boiling heat transfer deteriorates, probably because of increasing drop bouncing effects.

Acknowledgements

The present work was partly funded by the University of Palermo (former 60% – 2003 funds). The contribution of Dott. Ing. Gaetano Aiello in conducting the experimental measurements is gratefully acknowledged.

References

[1] D. Hall, I. Mudawar, Experimental and numerical study of quenching complex-shaped metallic alloys with multiple, overlapping sprays, Int. J. Heat Mass Transfer 38 (1995) 1201–1216.
[2] V. Brucato, S. Piccarolo, G. Titomanlio, Crystallization kinetics in relation to polymer processing, Macromol. Chemie – Macromol. Symp. 68 (1993) 245.
[3] C.H. Amon, J. Murthy, S.C. Yao, S. Narumanchi, C.-F. Wu, C.-C. Hsieh, MEMS-enabled thermal management of high-heat-flux devices EDIFICE: embedded droplet impingement for integrated cooling of electronics, Exp. Thermal Fluid Sci. 25 (2001) 231–242.
[4] G.P. Celata, M. Cumo, A. Mariani, L. Saraceno, Heat flux and heat transfer coefficient in quenching of hot surfaces by drop impingement, in: Proc. 13th International Heat Transfer Conference (IHTC-13), Sydney, Australia, 13–18 August 2006.
[5] L. Bolle, J.C. Moureau, Spray cooling of hot surfaces, in: G.F. Hewitt, J.M. Delhaye, N. Zuber (Eds.), Multiphase Science and Technology, Hemisphere, Washington, 1982, pp. 1–97.
[6] N. Dombrowski, G. Munday, Spray Drying, Biochemical and Biological Engineering Science, vol. 2, Academic Press, London, 1968.
[7] E. Babinsky, P.E. Sojka, Modeling drop size distributions, Progress Energy Combust. Sci. 28 (2002) 303–329.
[8] R.A. Mugele, H.D. Evans, Droplet size distribution in sprays, Ind. Eng. Chem. 43 (6) (1951) 1317–1324.
[9] G. Brenn, T. Helpio, F. Durst, A new apparatus for the production of monodisperse sprays at high flow rates, Chem. Eng. Sci. 52 (1997) 237–244.
[10] R. Clift, J.R. Grace, M.E. Weber, Bubbles, Drops, and Particles, Academic Press, New York, 1978.
[11] C.F. Weber, Analysis and solution of the ill-posed inverse heat conduction problem, Int. J. Heat Mass Transfer 24 (1981) 1783–1792.
[12] J. Taler, Theory of transient experimental techniques for surface heat transfer, Int. J. Heat Mass Transfer 39 (1996) 3733–3748.
[13] C.J. Hoogendoorn, R. den Hond, Leidenfrost temperature and heat transfer coefficients for water sprays impinging on a hot surface, in: Proc. 5th International Heat Transfer Conference, IV, Japan Soc. Mech. Eng. Soc. Chem. Eng., Tokyo, 1974, p. 135.
[14] H. Junk, Wärmeübergangsuntersuchungen an einer simulierten Sekundärkühlstrecke für das Stranggiessen von Stahl, Neue Hütte 1 (1972) 13–18.
[15] H. Müller, R. Jeschar, Untersuchung des Wärmeübergangs an einer simulierten Sekundärkühlzone beim Stranggiessverfahrer, Arch. Eisenhüttenwes 1 (1973) 589–594.
[16] K.J. Choi, S.C. Yao, Mechanisms of film boiling heat transfer of normally impacting spray, Int. J Heat Mass Transfer 30 (1987) 311–318.

[17] S. Deb, S.C. Yao, Analysis on film boiling heat transfer of impinging sprays, Int. J. Heat Mass Transfer 32 (1989) 2099–2112.
[18] M. Ghodbane, J.P. Holman, Experimental study of spray cooling with Freon-113, Int. J. Heat Mass Transfer 34 (1991) 1163–1174.
[19] M. Ciofalo, I. Di Piazza, V. Brucato, Investigation of the cooling of hot walls by liquid water sprays, Int. J. Heat Mass Transfer 42 (1999) 1157–1175.
[20] S. Puleo, Studio sperimentale dello spray cooling di pareti calde, Doctoral dissertation, Department of Nuclear Engineering, University of Palermo, 2005 (in Italian).
[21] NIST (National Institute of Standards and Technology), Temperature-electromotive force reference functions and tables for the letter-designated thermocouple types based on the ITS-90, U.S. NIST Monograph 175, 1993 (online at <http://srdata.nist.gov/its90/main/>).
[22] S. Puleo, A. Caronia, M. Di Liberto, M. Ciofalo, Induction heating of planar aluminum targets for spray cooling research, in: Proc. 60th National Conference of ATI (Associazione Termotecnica Italiana), Rome, Italy, 13–15 September 2005.
[23] D.R. Lide, Handbook of Chemistry and Physics, CRC Press, London, UK, 1995.
[24] J. Stefan, Über die Theorie der Eisbildung insbesondere über Eisbildung im Polarmeere, Sitzungsberichte der Kaiserlichen Akademie Wiss, Wien, Math. Natur. 98 (1889) 965–983.
[25] H.S. Carslaw, J.C. Jaeger, Conduction of Heat in Solids, second ed., Oxford University Press, Oxford, UK, 1959.
[26] M. Ciofalo, A. Caronia, M. Di Liberto, S. Puleo, On the derivation of the boiling curve in spray cooling from experimental temperature–time histories, in: Proc. 13th International Heat Transfer Conference (IHTC-13), Sydney, Australia, 13–18 August 2006.